Available online at www.sciencedirect.com
ScienceDirect
Journal of Computational Physics 227 (2008) 4912–4933
JOURNAL OF COMPUTATIONAL PHYSICS
www.elsevier.com/locate/jcp

# An implicit method for coupled flow–body dynamics

Silas Alben

*School of Mathematics, Georgia Institute of Technology, 686 Cherry Street, Atlanta, GA 30332-0160, United States*

Received 16 December 2006; received in revised form 21 August 2007; accepted 16 January 2008
Available online 26 January 2008

**Abstract**

We propose an efficient method for computing coupled flow–body dynamics. The time-stepping is implicit, and uses an iterative method (preconditioned GMRES) to solve the flow–body equations. The preconditioner solves a decoupled version of the equations which involves only the inversion of banded matrices, and requires a small number of iterations per time step. We use the method to probe the instability to horizontal motions of an elliptical body with simple vertical motions: flapping and rising. In both cases a linear instability to horizontal motion sets in above a critical Reynolds number, leading to a stable oscillatory state. The pressure forces play a destabilizing role against the stabilizing viscous forces, with oscillatory time scales set by either external flapping or the intrinsic flow–body coupling. The latter lowers the instability threshold in Reynolds number.


*PACS:* 47.11.–j; 47.11.Bc; 47.20.Ky; 47.63.M–

*Keywords:* Implicit; Coupled; Flow–body; Iterative; Decoupled; Preconditioner; Critical Reynolds number; Flapping

## 1. Introduction

Many problems of recent interest in biolocomotion involve the dynamics of fully-coupled flow–body systems [1–4]. When the motion of a fluid–solid boundary is not prescribed, but is instead determined in terms of the fluid forces on it, traditional methods for computational fluid dynamics face additional stability constraints.

Here we consider unsteady two-dimensional incompressible fluid flows, described by the Navier–Stokes equations. Among the many formulations used in numerical schemes, we focus on the finite-difference "vorticity–stream-function" formulation, one of the most widely-used. Over the past 80 years, most discussions of this formulation in the literature deal with the appropriate method for imposing the velocity boundary conditions (no-slip and no-penetration) on the vorticity–stream-function system [5]. The discretized boundary conditions exert a determining influence on both the accuracy and stability of the scheme, and often the former is decreased to enhance the latter [6]. For explicit schemes, stability requires that the time step be less than

*E-mail address:* alben@math.gatech.edu

0021-9991/$ - see front matter © 2008 Elsevier Inc. All rights reserved.
doi:10.1016/j.jcp.2008.01.021

a constant times the square of the smallest mesh spacing (the CFL condition), times the Reynolds number. Such schemes have recently been developed to study high-Reynolds-number flows [7] ($Re = 10^3 - 10^6$), and used in studies of flapping flight [8]. Typically the time step is $10^{-6} - 10^{-4}$ in these studies, where 1 is the time scale of external forcing (such as the flapping period of a wing). Thus a large computational expense is required to compute only a few flapping periods. When the motion of the body is not prescribed as in the above studies, but coupled to fluid forces, the CFL bound on the time step becomes even more strict, now involving the cube, not the square, of the smallest mesh spacing. Anderson et al. studied the falling of a plate coupled to a viscous fluid using an explicit scheme [9]. The dynamical properties of the system were predicted based on a small number of tumbling periods, but longer runs would have made the results more conclusive.

In such cases the time step required for stability is many orders of magnitude smaller than that required for high accuracy, and implicit schemes become more attractive. Such schemes involve the solution of a sparse matrix equation representing the coupled system with derivatives discretized using finite differences. As the matrix is sparse, iterative methods are generally more efficient than a direct solution, particularly when an effective preconditioner can be found.

Here we propose an implicit, iterative method for computing flow–body interactions. The amount of work required for each iteration scales as the number of grid points, which is of the same order as the work required for one time step of an explicit scheme [7]. Hence the implicit scheme is more efficient than the explicit scheme when the number of time steps decreases by a larger factor than the number of iterations. In our method, the number of iterations per time step ranges from 20 to 100, while the size of stable time steps can increase by a factor of $10^4$ or more, resulting in a decrease in computational time of a factor of more than 100. We give results of the method for studies of flow–body interactions at moderate Reynolds number ($10$–$10^2$), which are useful for understanding the behavior of bodies at the transition from low- to high-Reynolds number fluid dynamics [10], including the locomotion of small insects [11] and copepods [12]. However, the method is not inherently limited to this range of Reynolds number.

In Section 2, we give the vorticity–stream-function equations and boundary conditions in an infinite plane, written in terms of a boundary-fitted elliptic mesh. In Section 3, we give the implicit iterative scheme, which is designed to be closely approximated by a preconditioner matrix which is easy to solve. We use an operator splitting to write the unsteady and viscous terms as pentadiagonal matrices. Essential to the rapid convergence of the iteration is the preconditioner, which approximates the full system of equations by a decoupled block-matrix system. Hence the equations coupling boundary vorticity to the bulk flow, and to the motion of the body, are omitted in the preconditioner. Nonetheless, we obtain convergence in a small number of iterations.

In Section 4, we give results for the dynamics of a wing with motion coupled to the ambient flow, over times of up to 100 flapping periods, and compare these dynamics with those of an untethered bluff body in a steady flow. Both cases are near the Reynolds number at which instability to transverse oscillations sets in. We present a detailed picture of the instability, including the destabilizing role of pressure forces versus the stabilizing role of viscous forces, and the presence of phase-locking. We also find a transition from regular oscillations to irregular motions as the Reynolds number increases. In the appendices we present convergence studies and validations of the current method using benchmark problems.

## 2. Coupled flow–body equations

We solve the 2-D Navier–Stokes equations for the motion of an incompressible, viscous fluid in the vorticity–stream-function formulation. These are written in terms of the vorticity $\omega$, the flow velocity $\mathbf{u} = u_1\hat{\mathbf{e}}_x + u_2\hat{\mathbf{e}}_y$ and the stream function $\psi$

$$\frac{\partial\omega}{\partial t} + \mathbf{u}\cdot\nabla\omega = \frac{1}{Re}\Delta\omega,$$
$$\Delta\psi = \omega,$$
$$\mathbf{u} = \nabla^{\perp}\psi = (-\partial_y, \partial_x)\psi.$$

We have given the equations in standard nondimensional form using the Reynolds number $Re = LU/\nu$ with the characteristic velocity $U$ and distance $L$ defined below for two specific problems. We formulate our method

for the particular case of the motion of an elliptical body in the infinite plane. Dynamics of elliptical bodies have been studied often in classical hydrodynamics [13] and in Navier–Stokes simulations [8,14–16]. The latter use an elliptical mesh which is related to the physical plane coordinates $(x, y)$ by

$$x + \mathrm{i}y = \cosh(\mu + \mathrm{i}\theta), \quad \mu \in [0, \infty), \quad \theta \in [0, 2\pi). \tag{1}$$

In $(\mu, \theta)$ coordinates the Navier–Stokes equations may be written

$$S\frac{\partial \omega}{\partial t} + \nabla^{\perp}\psi \cdot \nabla\omega = \frac{1}{Re}\Delta\omega, \tag{2}$$

$$\Delta\psi = S\omega, \tag{3}$$

where now $\nabla = (\partial_\mu, \partial_\theta)$, $\Delta = \partial_{\mu\mu} + \partial_{\theta\theta}$, $\mathbf{u} = u\hat{\mathbf{e}}_\mu + v\hat{\mathbf{e}}_\theta$, and $S = \cosh^2\mu - \cos^2\theta$. For general coordinate transformations, $S$ is the Jacobian determinant of the transformation.

We consider rigid translational motions of the ellipse with velocity $(V_x, V_y)$, and solve the equations in a body-fixed frame. In this frame, the flow velocity $\sim (-V_x, -V_y)$ in the far-field, and is zero on the ellipse.

The boundary conditions for the Navier–Stokes equations (2) and (3) are zero flow velocity on the boundary of the ellipse ($\mu = \mu_0$), and translational flow at infinity. In terms of $\psi$ these conditions are

$$\begin{aligned} &\psi = \partial_\mu\psi = 0 \quad \text{for } \mu = \mu_0, \quad \theta \in [0, 2\pi), \\ &\psi \sim V_x \sinh\mu \sin\theta - V_y \cosh\mu \cos\theta, \quad \mu \to \infty. \end{aligned} \tag{4}$$

We consider two simple cases of motion: a body flapping with amplitude $A$ and frequency $f$, for which

$$V_y = 2\pi f A \sin(2\pi f t), \quad t \geqslant 0 \tag{5}$$

and a body rising at speed $V$, for which

$$V_y = V, \quad t \geqslant 0. \tag{6}$$

In both cases the horizontal motion is not prescribed, but is instead coupled to the horizontal component of the fluid forces

$$m\frac{\mathrm{d}V_x}{\mathrm{d}t} = F_{x,\mathrm{fluid}} = \hat{\mathbf{e}}_x \cdot \int_{\mathrm{body}} \mathbf{T}\cdot\mathbf{n}\,\mathrm{d}s, \tag{7}$$

where $m$ is the mass of the body, $\mathbf{n}$ is the unit normal vector on the surface of the ellipse, and $s$ is arc length. Here $\mathbf{T}$ is the fluid stress tensor for the Navier–Stokes equation,

$$\mathbf{T} = -p\mathbf{I} + \rho\nu(\nabla\mathbf{u} + \nabla\mathbf{u}^{\top}), \tag{8}$$

where $p$ is the pressure, $\mathbf{I}$ the identity matrix, $\rho$ the fluid area density and $\nu$ the kinematic viscosity.

In Eq. (7), we can write the terms involving $p$ and $\mathbf{u}$ in terms of $\omega$ and $\partial\omega/\partial\mu$ (see Appendix A). Then Eq. (7) becomes

$$\frac{\mathrm{d}V_x}{\mathrm{d}t} = \frac{\rho\nu}{m - \rho A_0}\int_0^{2\pi}(-\omega\cosh\mu_0\sin\theta + \partial_\mu\omega\sinh\mu_0\sin\theta)\mathrm{d}\theta. \tag{9}$$

For the case of flapping motion (Eq. (5)), we nondimensionalize by $\omega = f\tilde{\omega}$, $\mathrm{d}V_x/\mathrm{d}t = f^2 A\,\mathrm{d}\tilde{v}_x/\mathrm{d}\tilde{t}$. For the rising motion, we nondimensionalize using $\omega = (V/L)\tilde{\omega}$, $\mathrm{d}V_x/\mathrm{d}t = (V^2/L)\mathrm{d}\tilde{v}_x/\mathrm{d}\tilde{t}$. Inserting the nondimensional quantities and then dropping the tildes, Eq. (9) becomes

$$\frac{\mathrm{d}V_x}{\mathrm{d}t} = \frac{1}{M\cdot Re}\int_0^{2\pi}(-\omega\sin\theta/2 + \partial_\mu\omega\tanh\mu_0\sin\theta/2)\mathrm{d}\theta. \tag{10}$$

where $M = (m - \rho A_0)/\rho L^2$ and $Re = fAL/\nu$ (for flapping), $LV/\nu$ (for rising). There are two nondimensional parameters in this equation. The first is $M$, the body mass minus displaced fluid mass, divided by the fluid mass which lies approximately within the region swept out by the body in one period of vertical flapping. The second is the Reynolds number $Re$ which characterizes the balance of viscous and inertial fluid terms in the Navier–Stokes equation. Two additional parameters are the aspect ratio of the body, $\tanh\mu_0$, and $A/L$, the amplitude divided by the chord, which we set to 1/2 for the results shown subsequently.

The unknowns are the values of $\omega$ and $\psi$ on the $(\mu-\theta)$ grid and $V_x$. We now describe how the coupled flow–body equations (2), (3) and (10) and boundary conditions (4) are solved numerically.

## 3. The numerical method

The main element of our method is the implicit time discretization of the equations and the iterative method used to solve them. When the vorticity evolution Eq. (2) is discretized explicitly in time, the time step must satisfy $\Delta t < cRe\Delta x^2$ for stability. Here $\Delta x$ is the smallest spacing between mesh points and the constant $c$ has been estimated numerically as 1.5 [17]. To avoid this constraint we use an implicit time discretization.

The earliest implicit algorithms used relaxation methods, for which convergence is difficult to achieve, particularly for high-order boundary conditions [6]. More recent methods have used Krylov-subspace methods, though a large number of iterations is often needed for convergence [17]. Here we solve the $\omega-\psi$ system implicitly using the iterative solver GMRES [18] with a block-matrix preconditioner. For the particular preconditioner we use, convergence to $10^{-12}$ accuracy is obtained in a reasonable number of iterations— 20–100 depending on the flow parameters and the problem size. The iterative method is described in Section 3.4.

Two other aspects of Eqs. (2) and (3) are important for their numerical solution

1. The advection term in Eq. (2) is nonlinear.
2. On the body, there are two boundary conditions for $\psi$ and none for $\omega$.

The first aspect requires either a nonlinear solver, such as a Newton-type method, or else a quasi-linearization. We adopt the latter approach. The second aspect may be addressed by formulating the equation solely in term of $\psi$, with a biharmonic operator [19] or with finite elements in a variational formulation [20]. A Newton-type method has been used to solve the resulting nonlinear system [21]. This approach has been used mainly for steady problems, due to the large expense of forming and factoring the Jacobian matrix. Also, the discretized biharmonic operator yields a poorly-conditioned system which typically results in slow convergence. We use the more common approach of solving the Laplace operators in the two Eqs. (2) and (3) separately. A boundary condition for the vorticity on the body is then required; we use the well-known "Briley's formula", as described in Section 3.2.

The spatial discretization is a spectral-finite-difference scheme, which uses fourth-order difference stencils. In practice we find convergence between third and fourth order, which may be due to the discretization of $\partial_\mu\omega$, as described in Section 3.3.

Having outlined the relevant considerations for general finite-difference vorticity–stream-function schemes, we now describe our scheme.

### 3.1. Spatial discretization

We solve the problem on a two-dimensional grid: $\mu_j = \mu_0 + (\mu_B - \mu_0)j/n,\ j = 0,\ldots,n;\ \theta_k = 2\pi k/m,$ $k = 0,\ldots,m-1$. Fig. 1 shows the image in the physical plane of a mesh of points equally spaced in $\mu$ and

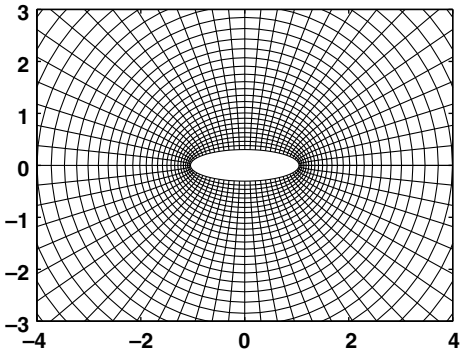


Fig. 1. The body fitted mesh.

$\theta$. Such a mesh provides good resolution near the body, which is important for computing the fluid forces on the body accurately. The mesh spacing increases with radial distance from the body. Hence it difficult to resolve significant vorticity far from the body, which can occur when the body travels far from its initial position.

The contour $\mu = \mu_0 =$ constant defines an ellipse with aspect ratio $\tanh \mu_0 \in [0, 1)$. We label the values of the stream function and vorticity computed at each point $(\mu_j, \theta_k)$ as $\psi_{j,k}$ and $\omega_{j,k}$. We perform the $\mu$-derivatives in Eqs. (2) and (3) using fourth-order-accurate finite-difference stencils, which are one-sided for mesh points near the boundaries. We perform the $\theta$-derivatives using Discrete Fourier Transform representations of $\omega$ and $\psi$ for each $\mu_j$. Differentiation then corresponds to multiplication of the Fourier coefficients [22].

The equations are discretized on the interior $\mu$-lines: $\mu = \mu_1, \ldots, \mu_{n-1}$. Near the boundaries, the finite-difference stencils incorporate the boundary conditions.

### 3.2. Numerical boundary conditions

There are essentially four boundary conditions imposed in our numerical solution of the system (2) and (3): the values of $\psi$ and $\partial_\mu \psi$ on the body ($\mu = \mu_0$), and the values of $\psi$ and $\omega$ on a contour far from the body ($\mu = \mu_B$).

#### 3.2.1. Boundary conditions on the body

The condition that flow does not penetrate the body is imposed by setting

$$\psi_{0,k} = 0, \quad k = 1, \ldots, m. \tag{11}$$

The proper way to impose the no-slip boundary condition on the body in (4) has received much attention since Thom's formula was proposed in the 1930s [23]. The method we use is a fourth-order version known as Briley's formula [24]. This converts the no-slip condition into a formula for $\omega$ on the no-slip boundary, using the Poisson Eq. (3) discretized at a point at the boundary. The vorticity boundary condition allows one to solve the system (2),(3) by using boundary data for $\psi$ and $\omega$ in finite-difference stencils.

Briley's formula is

$$S\omega_{0,k} = \left(6\psi_{1,k} - \frac{3}{2}\psi_{2,k} + \frac{2}{9}\psi_{3,k}\right)/\Delta\mu^2, \quad k = 1, \ldots, m. \tag{12}$$

By inserting the exact solution for $\psi$ into the right side of Eq. (12) and expanding in a Taylor series at the boundary point, one sees that the formula is apparently only third-order accurate. However, using an asymptotic error expansion it has been shown [7] that the error is actually fourth-order, using an argument which depends upon the cancellation of error terms at the boundary. The intuitive reason is that the vorticity formula is a surrogate for the fourth-order no-slip condition contained in it [25]. Some workers prefer to avoid vorticity boundary conditions altogether, though E and Liu have shown that they are formally equivalent to stream-function boundary conditions, and reproduce known solutions for benchmark problems [7] (see Appendix B).

#### 3.2.2. Boundary conditions in the far field

We impose the far-field conditions on an ellipse $\mu = \mu_B$, far from the body. Under diffusion alone the vorticity decays exponentially with radial distance from the ellipse. However, because the mesh, and therefore the outer boundary, moves with the ellipse, it can eventually enter a region containing vorticity. This occurs when the ellipse translates from its initial position to the initial position of the outer boundary. We set the outer boundary distance sufficiently large to avoid this phenomenon, and set the vorticity to zero on the outer boundary

$$\omega_{n,k} = 0, \quad k = 1, \ldots, m. \tag{13}$$

It is of the order of machine precision $(10^{-16})$ in all results shown here.

On the outer boundary we set $\psi$ as

$$\psi_{n,k} = -V_y \cosh \mu_B \cos \theta_k + V_x \sinh \mu_B \sin \theta_k + c_0, \quad k = 1, \ldots, m, \tag{14}$$

where $c_0$ is a constant fixed by the circulation $\Gamma = \int \omega dA$. For purely rectilinear motion (i.e., without rotation), the circulation is constant in time, or zero for a flow started from rest (see Appendix C). We add the equation

$$\Gamma = 0 \tag{15}$$

to our system of equations to solve for the unknown $c_0$.

The error in the expression (14) for $\psi_{n,k}$ may be estimated by considering the exact solution $\psi$ expressed as a series in circular harmonics as in Anderson and Reider [26].

The error is $O(e^{-\mu_B})$, the size of the largest decaying term in the expansion of $\psi$ in circular harmonics. Since $\psi_{n,k}$ is $O(e^{\mu_B})$, the relative error is $O(e^{-2\mu_B})$, which in practice is of the order of 1% for boundary sizes of $\sim 10^2$ body radii. Higher accuracy may be obtained using an implicit correction similar to one given in [26]. The numerical error due to the outer boundary condition is shown to decay exponentially with $\mu_B$ in Appendix E.4.

### 3.3. Numerical equations

Having given the discrete form of the boundary conditions, we now give the discretized version of the flow–body equations (2) and (3). We use implicit time-stepping, and write the system to be well approximated by a preconditioner which involves solving only banded (diagonal and pentadiagonal) matrices.

Hence each application of the preconditioner has a computational cost which is linear in the number of grid points. We therefore use a splitting the viscous operator [27], and second-order time-stepping, to leave only banded matrices on the left-hand side of the discretized evolution Eq. (2). Denoting the current time step as $n+1$, the discretization of Eq. (2) is

$$\widetilde{S}^{-1}\left\{L_1 L_2 \omega^{n+1} + \frac{\Delta t}{2}\nabla^{\perp}[\psi]^{n:n-1}\cdot\nabla\omega^{n+1}\right\} = \widetilde{S}^{-1}\left\{\tilde{L}\omega^{n} - \frac{\Delta t}{2}\nabla^{\perp}[\psi]^{n:n-1}\cdot\nabla\omega^{n} + D\omega^{n}\right\}, \tag{16}$$

where the operators are defined by

$$\widetilde{S} = \cosh^2\mu - \frac{1}{2},$$
$$L_1 = S - \frac{\Delta t}{2Re}D_\theta^2,$$
$$L_2 = I - \frac{\Delta t}{2SRe}D_\mu^2,$$
$$\widetilde{L} = S + \frac{\Delta t}{2Re}(D_\theta^2 + D_\mu^2),$$
$$D = \left(\frac{\Delta t}{2Re}\right)^2 D_\theta^2\left(\frac{1}{S}D_\mu^2(\cdot)\right).$$

The discrete operator $D_\mu^2$ is fourth-order, and one-sided near the boundary, using $\omega_{0,k}$ from Eq. (12). The operator $L_1$ is written in physical space, as a pentadiagonal matrix acting on a column vector with entry in row $m(j-1)+k+1$ equal to $\omega_{j,k}$. The operator $L_2$ is also a pentadiagonal matrix, when the $\omega$ vector is reordered so that the entry in row $(n-1)k+j$ is equal to $\omega_{j,k}$ (as in the Alternating Directions Implicit, or ADI method [27]).

We obtain the expressions for $L_1$ and $L_2$ from the fact that they are the approximate factors of the diffusive part of Eq. (2), as in the ADI method. The $D$ operator is needed to cancel the difference between the product of $L_1$ and $L_2$ and the diffusive part. The nonlinear term is linearized in the lowest-derivative part, and discretized at the $n+1/2$ time step. The purpose of the $\widetilde{S}$ operator is to weight the equations, and therefore also the residual which is to be minimized, more strongly near the body, ensuring that errors there are made small by the iterative method. The operator $\widetilde{S}$ is also $\theta$-independent, so that its inverse is a diagonal rather than a dense matrix in Fourier space and may be inverted rapidly in the preconditioner.

Here $[\psi]^{n:n-1} = (3/2)\psi^n - (1/2)\psi^{n-1}$ is a second-order extrapolation to the $n+1/2$ step. Because two previous time levels are needed for this extrapolation, the first time step is solved with a Crank–Nicolson discretization, with the nonlinear term treated implicitly. We note the time discretization can easily be made higher

than second order. The second-order splitting can be limited to the preconditioner, whereas the full equations can be written at higher order, and still be sufficiently well approximated by the preconditioner not to significantly increase the iteration count. For the results we present below, the accuracy is more limited by the fourth-order spatial discretization than by the second-order time discretization. This is shown in Appendix E, where we give typical errors in computing benchmark quantities described in Section 4.

We note that the viscous term is written implicitly, and the nonlinear term is written implicitly in the highest-derivative part. The extrapolation in the second-order term could be expected to cause an instability for large time steps, but we find no noticeable instability for all choices of $Re$ and $\Delta t < 0.02$, where $t = 1$ is one flapping period (see Eq. (5)). For all of the results presented in this work, $\Delta t = 0.005$ is sufficient for 1% accuracy. (see Appendix E.3). The system may also be solved with a fully-implicit nonlinear term, but the inclusion of this nonlinearity increases the number of iterations required for convergence by 40–100%.

The Poisson Eq. (3) is discretized as

$$\widetilde{S}^{-1}\left\{(D_\mu^2 + D_\theta^2)\psi^{n+1} - S\omega^{n+1}\right\} = 0. \tag{17}$$

The horizontal momentum Eq. (10) is discretized as a second-order Backward Differentiation scheme

$$(3/2)V_x^{n+1} - 2V_x^n + (1/2)V_x^{n-1} = \Delta t F_{x,\mathrm{fluid}}^{n+1}. \tag{18}$$

The integral in $F_{x,\mathrm{fluid}}^{n+1}$ is discretized with the trapezoidal rule. To compute $\partial_\mu\omega$, we use the fourth-order one-sided stencil

$$\partial_\mu\omega_{0,k} \approx ((-25/12)\omega_{0,k} + 4\omega_{1,k} - 3\omega_{2,k} + (4/3)\omega_{3,k} - (1/4)\omega_{4,k})/\Delta\mu. \tag{19}$$

In the asymptotic error expansion for $S\omega_{0,k}$ in [7], the leading-order error term is $O(\Delta\mu^4)$, but it is not of the form $C\partial^6\psi/\partial\mu^6(\mu_0)\Delta\mu^4$, which is the form of the leading-order error terms in $S\omega_{j,k}, j = 1\ldots4$. Hence the stencil (19) is only third-order accurate in general. In our convergence studies we find that this error is between third- and fourth-order (see Appendix E). However, Pan and Chew have shown that the $\partial_\mu\omega$-term may be eliminated in favor of an integral term which involves only $\omega$ and an auxiliary function over the flow field (see [28]); this incurs some additional computational expense and we do not use this method here.

Conservation of circulation (Eq. (15)) is written

$$\sum_{j=0}^{n}\sum_{k=0}^{m-1} a_j S\omega_{j,k}^{n+1}\Delta\mu\Delta\theta = 0, \tag{20}$$

where the weights $a_j$ correspond to Simpson's rule for the $\mu$ index, and the trapezoidal rule in the $\theta$ index (which converges exponentially for analytic periodic functions, by the Euler–Maclaurin summation formula).

The full system of discretized equations consists of Eqs. (16)–(18), and (20), together with boundary conditions in Eqs. (11)–(14). The system may be written as $Ax = b$, where $A$ is a matrix of order $2m(n-1)+2$ multiplying the vector $x = (\omega_{j,k}, \psi_{j,k}, V_x, c_0)^{\mathrm{T}}, j = 1\ldots n-1, k = 1,\ldots,m$. The right hand side vector $b$ consists of the part of the boundary conditions which are known at each time step–the term in the outer boundary value of $\psi$ (Eq.(14)) containing $V_y$ (prescribed), and the values of $\psi$ on the body (Eq. (11)) and $\omega$ in the far field (Eq. (13)). All other terms in the equations and boundary conditions, including the flow–body coupling, appear in $Ax$.

The system is solved using GMRES [18], which requires only the multiplication of a vector by the matrix corresponding to the linear system of equations—in other words, the formation of the left-hand sides of Eqs. (16)–(20)–so the matrix is not formed explicitly. As $A$ is nearly banded, the computational work for each time step thus scales as the number of variables times the number of iterations needed to achieve convergence in GMRES, so the key factor in the efficiency of the method is the number of iterations. We now describe the preconditioner which requires a very small number of iterations, typically 20–100, in a wide range of flow conditions.

### 3.4. Preconditioning

A preconditioner is needed to make GMRES converge in a small number of iterations for this problem, because it has a large condition number due to the fourth-order discrete derivatives. A preconditioner replaces

the full linear system $Ax = b$ by $M^{-1}Ax = M^{-1}b$, and requires the solution of a linear system $Mv = w$ which is inexpensive to solve. Application of our preconditioner (i.e., calculation of $v = M^{-1}w$) consists of two steps.

(1) Given the part of $w$ representing the right side of Eq. (16), the three operators $\widetilde{S}^{-1}$, $L_1$ and then $L_2$ are inverted in sequence. $L_1$ is pentadiagonal in Fourier space, and $L_2$ is pentadiagonal, so the work of inversion is linear in the number of variables. The result is $\tilde{\omega}$, an approximation to $\omega$ at the current time step.
(2) $S\tilde{\omega}$ is formed by multiplication and added to the part of $w$ representing the right side of Eq. (17). Then $\psi$ is obtained as $\Delta^{-1}(S\tilde{\omega})$. The discrete Laplacian is inverted in Fourier space, where it is pentadiagonal for our fourth-order scheme.

Essential to note is that both the inner boundary condition for $\omega$ (Briley's formula (12)), and the force balance equation (Eq. (18)), both of which couple $\omega$ to $\psi$, are ignored in the preconditioner. This allows one to solve the $\omega$ and $\psi$ equations separately using sparse matrix methods. The iterative method of Iliev and Makarov [17] also ignored the vorticity boundary condition in the preconditioner. However, they used a different discretization of the equations and iterative method, and did not consider coupling between the flow and the body motion. Our preconditioner also ignores the nonlinear term in Eq. (16), and the equation enforcing conservation of circulation (Eq. (20)), which are assumed to be subdominant to the viscous term in their contribution to the spectrum of the full linear operator.

### 3.5. Time-stepping

We list the sequence of steps for a flow starting from rest.

(1) Initialization
  $t = 0$:
    Set $\omega^0 = 0$, $\psi^0 = 0$, $V_x^0 = V_y^0 = 0$.
(2) Time-stepping $t = \Delta t, 2\Delta t, 3\Delta t, \ldots$:

Solve the system of Eqs. (16), (17), (18), and (20), together with boundary conditions in Eqs. (11)–(14) using GMRES, with the preconditioner described in Section 3.4. Initialize the iteration with a first- or second-order extrapolation from solutions at previous time steps.

At the first time step $t = \Delta t$, make the nonlinear term fully implicit in Eq. (16), and substitute $V_x^1 = (\Delta t/2)F_{x,\text{fluid}}^1$ for Eq. (18) at this time step, retaining second-order accuracy.

We set the criterion for convergence in terms of the relative norm of the residual of the linear system: $||Ax - b||_2/||b||_2 \leqslant 10^{-12}$. The number of iterations required at each time step ranges from 20 to 100 depending on $Re$, $\Delta t$, the ellipse aspect ratio, and the system size. The overall work is significantly less than explicit schemes, which we explain in the next section. In our method, the number of iterations for convergence increases by 30–40% when both $m$ and $n$ are doubled. Thus the total work grows approximately as $N^{1.2}$ for $N$ variables, slightly faster than linearly.

### 3.6. Comparison with explicit schemes

Before presenting results on coupled flow–body dynamics, we compare our scheme with an explicit scheme in terms of the work involved for a benchmark problem. We consider ellipses of three aspect ratios, which are nearly neutrally-buoyant ($M = 0.001$), and which move vertically as $V_y = 1 - e^{-(t/0.02)^2}$. We use a moderate Reynolds number $Re = 5$ near the values used in the results section below. The horizontal motion $V_x$ is the same as the vertical motion for the first five time steps, after which it is coupled to the fluid according to Newton's Law (9). For this case, we discretize the equations of motion (2), (3) and (9) explicitly in time, using Euler's method. We obtain the values at time step $n + 1$ as

$$S\omega^{n+1} = S\omega^n - \Delta t \nabla^{\perp}\psi^n \cdot \nabla\omega^n + \Delta t \frac{1}{Re}\Delta\omega^n, \tag{21}$$

Table 1
Comparison of the time intervals computed per unit of computational work by implicit and explicit schemes for a range of aspect ratios, for the coupled motion of the fluid and a nearly neutrally-buoyant body ($M = 0.001$) at $Re = 5$

| Ellipse aspect ratio | Implicit number of iterations | Implicit $\frac{\Delta t}{2\times\text{number of iterations}}$ | Explicit $\Delta t_{\max}$ |
|---|---|---|---|
| 0.3 | 38 | $6.6 \times 10^{-5}$ | $4.8 \times 10^{-7}$ |
| 0.2 | 54 | $4.6 \times 10^{-5}$ | $6.8 \times 10^{-7}$ |
| 0.1 | 80 | $3.1 \times 10^{-5}$ | $1.2 \times 10^{-6}$ |

For three different aspect ratios (left column), the number of iterations needed to solve the discrete equations to $10^{-12}$ accuracy in the implicit scheme is given (second column). The implicit time step used to achieve 1% accuracy ($5 \times 10^{-3}$) is divided by twice the number of iterations to obtain the length of time covered by the implicit scheme for approximately the same amount of work as used in one time step of the explicit scheme. Hence, for the same amount of computational work, the third column gives the length of time computed by the implicit scheme, while the fourth gives the length of time computed by the explicit scheme. For higher accuracy of the implicit scheme, a fourth-order time discretization can be used.

$$\Delta\psi^{n+1} = S\omega^{n+1}, \tag{22}$$

$$V_x^{n+1} = V_x^n + \Delta t F^n_{x,\text{fluid}}. \tag{23}$$

The spatial discretization is unchanged from the implicit method. Different explicit schemes are stable at larger time steps than the Euler discretization given here, which we use for simplicity. However, the smallest unstable time step among different explicit schemes will differ by an order-1 constant, independent of the physical parameters $(Re, M)$.

The two matrix multiplications dominate the computational cost of each iteration of the implicit scheme, and each matrix multiplication is nearly equal in cost to one explicit time step. Hence the computational cost of one iteration of the implicit scheme is approximately twice the cost of one time step of the explicit scheme. The comparison we make, then, is between the time step of the explicit scheme, and the time step of the implicit scheme divided by the twice the number of iterations per time step.

The numerical parameters are: $m(= 2\pi/\Delta\theta) = 96$, $n = 96$, $\mu_B = 6$, which give approximately 1% accuracy for a range of aspect ratios $> 0.05$. In Table 1, we display the largest stable time steps in the explicit scheme, together with the time step in the implicit scheme divided by twice the number of iterations. We find that, for the same amount of computational work, the length of time computed by the implicit scheme is between 25 and 140 times that computed by the explicit scheme, depending on the aspect ratio.

For larger Reynolds numbers, we find that the largest stable time step in the explicit scheme is proportional to the Reynolds number, as is known from previous studies [38,7]. However, the mesh size needed to resolve the boundary layer must shrink at least as fast as the boundary layer thickness, proportional to $Re^{-1/2}$. Since the largest stable time step is also bounded above by the mesh spacing squared due to the diffusive term in Eq. (2), this factor contributes a term proportional to $Re^{-1}$ to the time step bound. This factor cancels the overall $Re$ factor, and consequently the largest stable time step for which the boundary layer is resolved is independent of $Re$. In other flow situations with Reynolds number $\gg 1$, the convective term may further restrict the largest stable time step for the explicit scheme.

## 4. Results

We begin by presenting the numerical solution for a particular case of a flapping body—a thick wing with density nearly that of the fluid. This solution illustrates some of the generic features we have found over a wide range of the parameter space. The system is initialized from rest, with a sinusoidal vertical flapping motion as in Eq. (5), with $f = 1$. The aspect ratio is 0.3 ($\mu_0 = 0.3$), $M = 1$, and $Re = 11$. The horizontal velocity $V_x$ is initially zero, and is coupled to the horizontal fluid forces for all time. The $O(10^{-16})$ round-off error in built-in trigonometric functions is a source of horizontal asymmetry, as is the sequence of forward and back substitution used to invert operators in the preconditioner. These errors result in a horizontal asymmetry of $O(10^{-12})$ in the flow and in $V_x$ after the iterations in the first time step.

In Fig. 2a we show $V_x$ versus time, and the corresponding trajectory of the center of mass. We see that the velocity remains small for the first 25 flapping periods, and then becomes order one, oscillating between $-3$

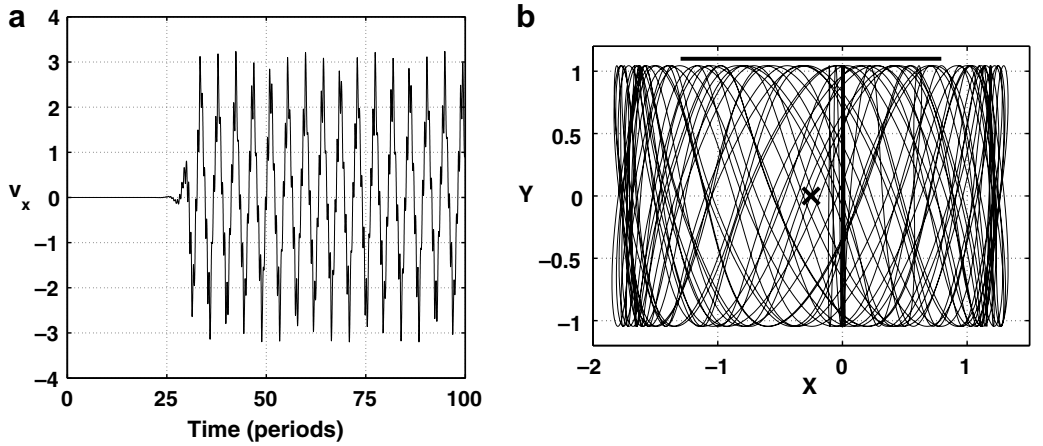


Fig. 2. The horizontal velocity and trajectory for $Re = 11$. (a) The horizontal velocity versus time. (b) The corresponding trajectory of the body center of mass. The black line above the plot represents the body length (chord). The mean horizontal position over the last 12 periods of $V_x$ is marked with a cross.

and 3 with a mean value which is slightly displaced from zero due to the startup conditions. The period of oscillation is very regular: the interpeak intervals are a repeating sequence of three intervals of duration $\Delta T = 4.510 \pm 0.005$ followed by one interval of duration $\Delta T = 3.980 \pm 0.005$; the variation 0.005 is the step size used in the computation. We note the proximity of these values to half-integer multiples of the flapping period. A plot of the frequency spectrum shows peaks at the two frequencies of this sequence, and at higher multiples. As we will show, the same behavior occurs when $V_x$ is initialized at O(1); hence, this horizontally-oscillating state appears to be an attractor of the system. Fig. 2b shows the corresponding trajectory of the body center of mass. The trajectory is nearly symmetric about the mean position.

In Fig. 3b we replot the first 40 periods of Fig. 2a on a log scale. The horizontal velocity apparently grows exponentially, with a linear envelope extending from $\pm 10^{-12}$ to order one. The horizontal velocity changes sign with approximately the same period as in the order-one regime. However, the exponential growth regime is different in that the velocity reverses sign multiple times in a brief span and then has one sign for a longer period. Fig. 3a and c show the same situation but with a lower $Re = 6.6$ and a higher $Re = 13$. We find no apparent growth at the smaller $Re$ and exponential growth at a higher rate at the higher $Re$. We also note that $V_x$ has constant sign at $Re = 6.6$, which seems to occur whenever there is no growth beyond the initial $O(10^{-12})$ asymmetry. However, the constant sign of $V_x$ may be positive or negative for different choices of $Re$ in the no-growth regime and for different initial conditions.

Fig. 4 shows the exponential growth rate plotted for a range of $Re$ at these parameters. There is apparently a critical $Re$ of 8.3 at which the instability begins.

There are two distinct regimes of body dynamics apparent in Figs. 2a and 3a–c.

(1) The linear instability regime, in which $V_x \ll 1$ and grows exponentially.
(2) The "saturated" regime, in which $V_x$ is order one and the body exhibits a quasi-periodic motion.

We now compare these results with those for a simpler system—an ellipse rising at constant speed $V$ instead of flapping (Eq. (6)), and again free to move horizontally. A similar problem for a rising sphere was studied by Jenny et al. [29]. For this problem we also find a linear growth regime, which is shown in Fig. 5a. Using $Re = LV/\nu$ we find $Re_{cr} = 23$, which is of the same order as the value for flapping, 8.3. Exact agreement is not expected, since the flapping velocity varies from 0 to $2\pi fA$. Consequently, $Re_{cr}$ for flapping could be taken as large as $2\pi \cdot 8.3 = 52$. We further note that the $Re_{cr}$ of 23 for the rising wing with free $V_x$ is below the critical value of 40 we have calculated for the instability to asymmetry of the wake for the same body, but fixed horizontally ($V_x = 0$). This is the threshold above which we first see exponential growth in $F_{x,\text{fluid}}$. Hence the coupling of body motion can lower the threshold for the generic instability of a wake flow past a fixed body.

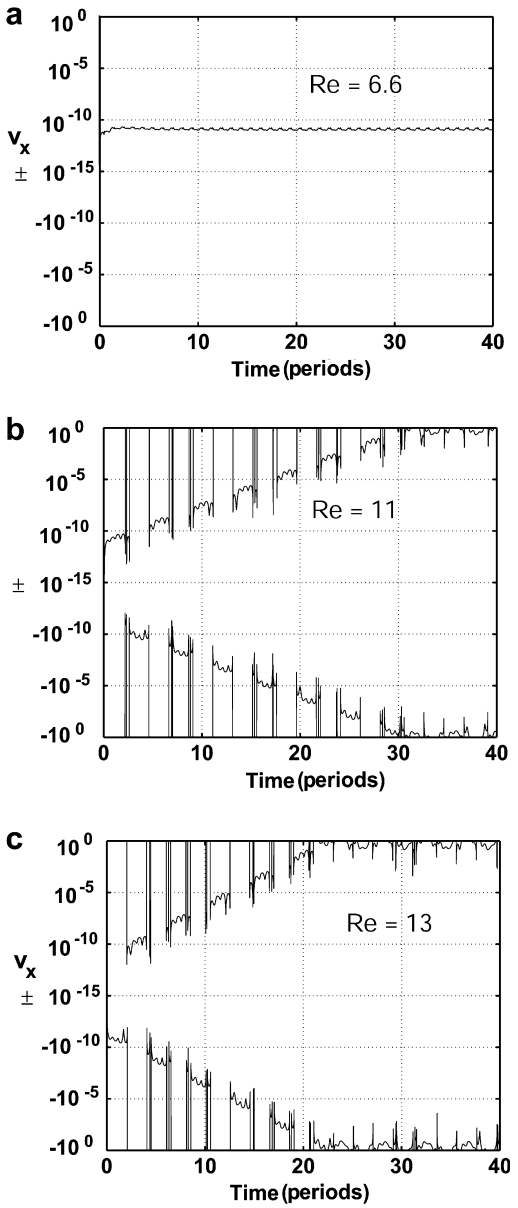


Fig. 3. The horizontal velocity versus time, on a log-linear scale, for $Re = 6.6$ ((a) top), $Re = 11$ ((b) middle), and $Re = 13$ ((c) bottom). For $Re = 6.6$ there is no discernable growth from the $10^{-12}$ level.

Because $Re_{cr}$ for a rising body is similar to that for the flapping body, the collision with previously-shed vortices in flapping probably plays a secondary role in the instability.

We also note that $V_x$ in the rising problem has a characteristic frequency which gives a Strouhal number of $St = fL/V = 0.04 - 0.08$ for $Re = 30 - 70$. Here $L$ is the chord length, $f$ is the frequency of the oscillations, and $V$ is the rising velocity. This is close to the range of $St$ for the vortex shedding about a fixed circular cylinder at these $Re$ [30]. In previous experimental studies of freely-rising bodies, von Kármán shedding has been shown to drive the instability of the free body [31,32]. Hence it is plausible that a von Kármán-type instability is also the driving instability for the flapping wing. However, the frequency of flapping introduces a time scale which is not present for the freely-rising body, and this accounts for the differing temporal structures between Figs. 5a and 3.

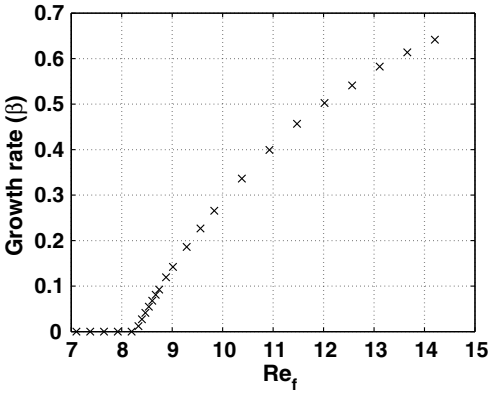


Fig. 4. The exponential growth rate corresponding to the envelopes of the curves in Fig. 3a and c, which have the apparent form $V_x = v_0 10^{\beta t}$. The growth rate is plotted versus $Re$, and indicates a critical $Re = Re_{cr}$ of 8.3 for these parameters.

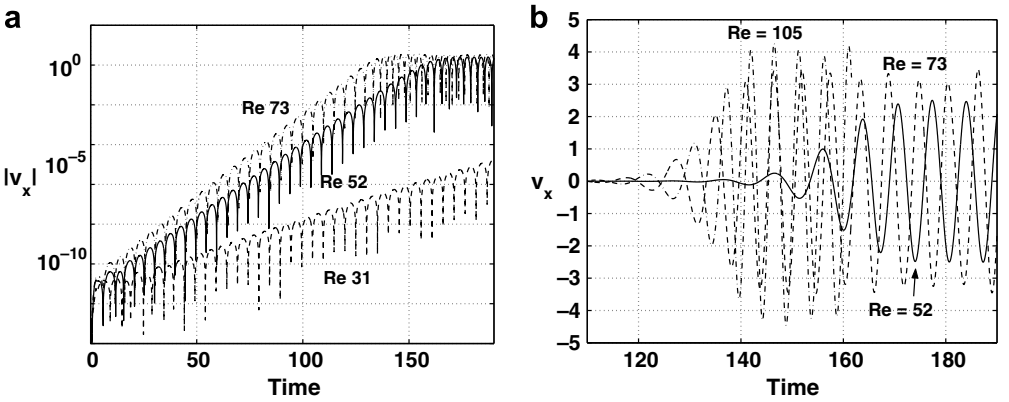


Fig. 5. The linear growth and saturated regimes for the rising problem. In both cases the behavior is similar to the flapping problem, except for the time scales of oscillation.

In Fig. 5b we show $V_x$ in the saturated regime for the free rising problem. We see that the peak values of $V_x$ increase with $Re$, and correspond to a horizontal amplitude on the order of the body chord, as in the flapping case (see Fig. 2a.) Similar dynamics were found for a cylinder by Shiels et al. [33]. The period of oscillation of $V_x$ is different from that of the flapping case, again because there is no flapping frequency. The qualitative similarity with the flapping case shows that flapping is not necessary to generate large-scale oscillations.

Now we give more detail about the fluid dynamics present during the instability, in terms of the fluid forces on the body. In Fig. 6 we show the viscous and pressure forces, as well as the horizontal velocity, through the transition of $V_x$ from linear growth to saturation, for rising (a) and flapping (b). We begin with the simpler rising case. Here $Re = LV/\nu = 52$ and $M = 1$. The linear growth regime has a dominant frequency corresponding to $St = 0.10$, close the von Kármán frequency at this $Re$. $St$ increases sharply to 0.14 when the body enters the saturated regime. The pressure force is slightly ahead of $V_x$ in temporal phase. After the peak of $V_x$ in each period, the pressure force changes from thrust to drag, and continues to accelerate the body in the opposite direction as $V_x$ crosses zero and peaks again with opposite sign. The viscous force is almost exactly opposite to $V_x$ in phase, and thus acts as a drag throughout the motion. It is interesting to note that in the saturated regime, the viscous and pressure forces have essentially the same roles.

The flapping dynamics (Fig. 6b) are shown for $Re = 13$, $M = 1$, and are significantly more complicated. Generally, as for pure rising, the pressure force is slightly ahead of $V_x$ in phase, while the viscous force has the opposite phase. However, both forces change sign on smaller time scales than $V_x$. For the thick wing used here (aspect ratio 0.3), viscous and pressure forces are of nearly the same magnitude in both regimes. However,

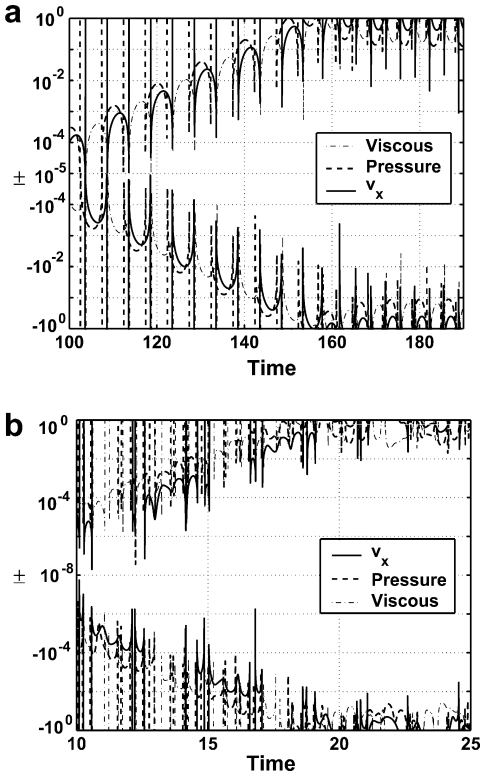


Fig. 6. The horizontal velocity, pressure and viscous forces in the linear growth and saturated regimes, for rising ((a), top) and flapping ((b), bottom). We omit the values between $-10^{-8}$ and $10^{-8}$.Time is in units of $L/V$ and flapping periods, respectively.

a preliminary study has shown that for a much thinner wing (aspect ratio 0.01), viscous forces are dominant in the saturated regime, and thus provide both drag and thrust.

In Fig. 7 we show more of the temporal structure of the dynamics in Fig. 6. Plotted are the time intervals between zero crossings of viscous and pressure forces, marked at the end of the interval. For the rising body, the transition from the linear growth to saturated regimes may be seen starting at $t = 150$ in Fig. 6a. In Fig. 7a we see that in each regime there is essentially a single characteristic time scale for the dynamics. For the flapping body, the analogous plot (Fig. 7b) is more complicated. Here $V_x$ saturates at $t \approx 22$, but there is a much longer transition period, $22 \lesssim t \lesssim 40$, before the flow periods reach a quasi-steady state. We again note that the flapping time scale is apparent, in the proximity of the longer time intervals to multiples of 0.5 throughout the dynamics.

### 4.1. The saturated regime

Having discussed the linear instability regime, and the temporal structure of the transition to saturation, we will now focus on the quasi-periodic dynamics of the system when $V_x$ saturates. The parameters are the same as for Fig. 2 ($Re = 11, M = 1$), but this time $V_x$ is set to $1 - e^{-(t/0.2)^2}$ for $0 \leqslant t < 0.5$, and is then set by fluid forces for $t \geqslant 0.5$, in order to initiate the saturated regime more quickly. The horizontal velocity is shown in Fig. 8a, and despite the different initial condition, the dynamics are similar to that in Fig. 2a for $t > 27$. In the present case, the first four periods of $V_x$ starting at $t = 6.2$ have duration $T = 3.995 \pm 0.005$. We see again that the horizontal motion (and the fluid flow) is periodic at an integer multiple (or in the earlier case with zero initial $V_x$, a half-integer multiple) of the flapping period. This resembles the "lock-in" phenomenon of flow-induced vibration, in which the frequency of vortex shedding changes from the von Kármán frequency for a static body to coincide to that of the flow–body oscillation [34].

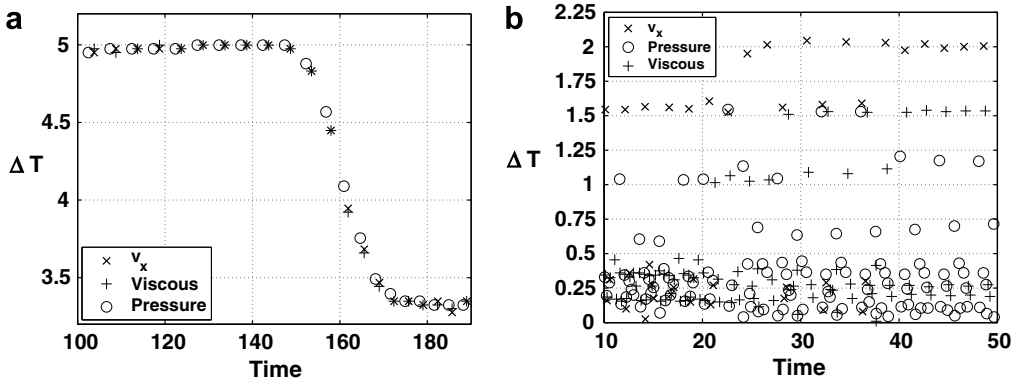


Fig. 7. The characteristic time periods of flapping and rising. Shown are the time intervals $\Delta t$ between consecutive zero crossings in $V_x$, the pressure force, and the viscous force, for the dynamics shown in Fig. 6. Values are marked at the end point of the interval. These time intervals represent the characteristic periods of the flow–body dynamics. For rising, there is a single characteristic period which undergoes a sharp transition when the amplitude of body oscillations becomes of the order of the chord length. For flapping, there are many characteristic periods, apparently close to integer multiples of the one-half period of flapping. Here a partial transition to longer periods occurs when the horizontal motion becomes of the order of the body chord length.

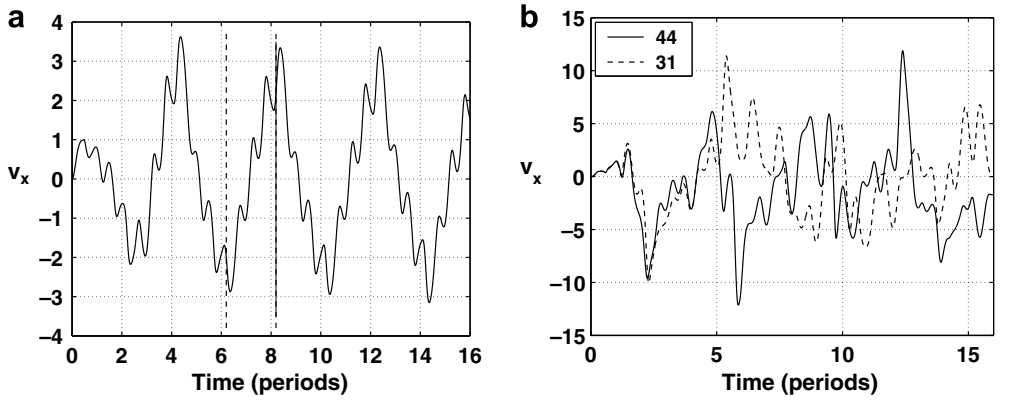


Fig. 8. (a) The horizontal velocity for $Re = 11$ in the saturated regime; $V_x$ is ramped up to 1 at $t$=0.5 and then released. The vertical dashed lines mark $t = 6.2$ and $t = 8.2$, the starting and ending points for Fig. 9. (b) The same situation but with $Re = 31$ and $Re = 44$. The dynamics are now much less regular.

Because the wing moves back and forth in a manner which is nearly symmetric, it is sufficient to describe the dynamics over a half-period (duration $T = 2$). In Fig. 9 we show the flow field at six instants, from $t = 6.2$ to $t = 8.2$. In this span of time (between the dashed vertical lines in Fig. 8a), the wing accelerates leftward, then decelerates, comes to a stop, and accelerates rightward. In each frame the instantaneous velocity of the wing is indicated by an arrow on the wing, and the values of the maximum and minimum vorticity on the surface of the wing are shown. Vorticity contours are logarithmically-spaced, given for decreasing powers of two in magnitude. Values of vorticity on the secondary vortices are also marked.

(1) In the first frame ($t = 6.2$), the wing is accelerating leftward. The vorticity is largest on the top side of the wing. The leftward and rightward components of pressure force are nearly in balance, but there is a significant viscous force pulling the wing to the left, from the large region of positive vorticity on the top left part of the wing.
(2) In the second frame ($t = 6.5$), the wing reaches its vertical maximum, and now has a large *rightward* acceleration. This is due to a strong rightward pressure force, as the vorticity at the trailing edge is nearly twice as large as at the leading edge. The intensity of the incipient trailing edge vortex (TEV) may be attributed to the action of the large negative leading edge vortex (with vorticity contour $-18$) which was swept past it between the first two frames.

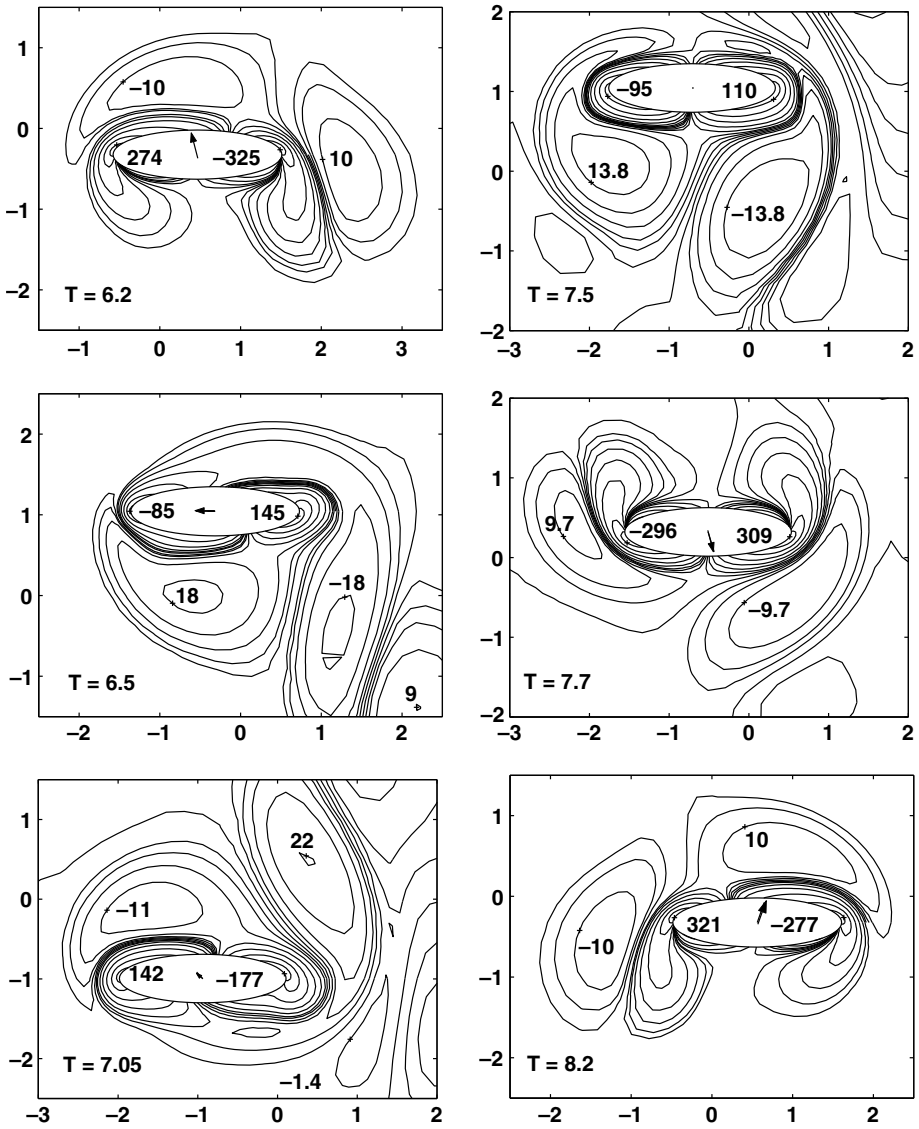


Fig. 9. The flow fields corresponding to one half-period of $V_x$ oscillation. Starting at the top left and moving down, then to the right, are isolines of vorticity at $t = 6.2$, $t = 6.5$, $t = 7.05$, $t = 7.5$, $t = 7.7$, and $t = 8.2$.

(3) The third frame ($t = 7.05$) shows the wing slightly more than a half-period ahead in time. The same distribution of forces as in the second frame decelerates the wing: a pressure low at the trailing edge, created by the large positive TEV from the previous frame. However, the difference in vorticity at the two edges is not as great as in the second frame, so the deceleration is reduced.
(4) In the fourth frame ($t = 7.5$), the wing is nearly stopped (at the top of the stroke and the leftward extreme in position), and there continues to be a rightward acceleration.
(5) In the fifth frame ($t = 7.7$), the moment of maximum rightward acceleration, the vorticity is nearly in balance yet there is a significant pressure drop at the right end. The acceleration is produced by a nearly even balance of pressure and viscous forces.
(6) In the sixth frame ($t = 8.2$), the wing continues to accelerate rightward by viscous forces on its top surface. The flow is nearly a mirror-image of that in the first frame.

Fig. 8b shows $V_x$ for two values of higher $Re$ (31 and 44) with the same start-up and all other parameters the same. The instants of vortex shedding can be seen clearly as the local extrema on the plot, spaced a half-period apart. At these larger $Re$, the peak values of $V_x$ are much larger, and a single shed vortex contains enough momentum to change the horizontal velocity from its peak value to a velocity of opposite sign. In the $Re = 11$ case, more than one shedding incident is required to change the sign of $V_x$ (as can be seen in the distance between the small peaks in Fig. 8a). At these higher $Re$, the body continually encounters previously-shed vortices which still have significant strength. It is known that a system of four or more point vortices can exhibit chaotic dynamics [35], so here the previously-shed vortices are expected to contribute to the irregularity of the dynamics. By contrast, for the $Re = 11$ case, a calculation of the fluid forces based only on the instantaneous body velocity may be sufficient to predict the dynamics.

The error in our scheme comes from two sources: the spatial and temporal discretization errors; and the error in the iterative method, defined by the size of the residual $||Ax - b||_2/||b||_2$ when convergence is achieved, as given in Section 3.3. The spatial errors are found to decay exponentially in $\Delta\theta$ and between third and fourth order in $\Delta\mu$ (see Appendix E.1), which is the limiting parameter for accuracy.

In Appendix D we compare the results of our scheme with those in the literature for steady flow past an oblique ellipse. We find agreement to within 1–2% in force coefficients.

## 5. Summary and conclusions

We have presented a new implicit numerical method for solving for coupled flow–body dynamics. The method avoids the time-step constraint for stability associated with explicit schemes, reducing the overall computational time by one to two orders of magnitude. The discrete equations are written to be well approximated by an efficient preconditioner. The key elements are: (1) an operator splitting, which allows second-order time accuracy while only banded diagonal matrices need to be inverted in each application of the preconditioner, (2) a preconditioner which decouples the solution of the vorticity evolution and stream function equations, by ignoring the vorticity boundary condition and the equation coupling the flow to the body motion, and (3) a scale factor which gives higher weight to terms near the body surface, where accuracy is most important.

We have applied our method to the coupled flow–body dynamics of a flapping ellipse and a rising ellipse. We have probed the instabilities to horizontal motion in the regimes of linear growth, and order-1 oscillations, which develop over long times. We find strong evidence of phase-locking in the horizontal motion of the flapping body, and deduce the destabilizing contribution of pressure and the stabilizing contribution of viscous forces in the dynamics. The rising body shows a similar oscillatory horizontal motion, which lowers the onset to horizontal asymmetry of the flow–body system. At higher $Re$, irregular dynamics are seen, corresponding to interactions of the body with multiple strong vortices.

## Acknowledgements

We would like to acknowledge Michael Shelley, Jun Zhang, and Stephen Childress for helpful discussions, and support of the Department of Energy (Grant No. DE-FG02-00ER25053).

## Appendix A. Coupled motion equation

Here we show how to express the integral in Eq. (7) in terms of $\omega$ and $\partial\omega/\partial\mu$. First, we write $x$ and $y$ as functions of the local orthogonal coordinates $n$ and $s$, normal and tangential to the body surface, respectively. Using incompressibility, the definition of vorticity, and $\mathbf{u} = 0$ on the body, we have

$$(\nabla\mathbf{u} + \nabla\mathbf{u}^\top)\cdot\mathbf{n} = \omega\mathbf{s} - \partial_s\mathbf{u} = \omega\mathbf{s}. \tag{A.1}$$

Now we express the pressure in terms of the vorticity. In the body frame, the flow velocity evolves according to

$$\rho\left(\frac{\partial\mathbf{u}}{\partial t} + \mathbf{u}\cdot\nabla\mathbf{u}\right) = -\nabla p + \rho\nu\Delta\mathbf{u} - \rho\frac{\mathrm{d}\mathbf{v}}{\mathrm{d}t}. \tag{A.2}$$

On the body surface the terms on the left are zero. Taking the tangential component of the remaining terms, we have

$$\partial_s p = \rho v \partial_n \omega - \rho \mathbf{s} \cdot d\mathbf{v}/dt, \quad \text{or} \tag{A.3}$$

$$p(s) = \rho v \int_0^s \partial_n \omega ds - \rho(\mathbf{x}(s) - \mathbf{x}(0)) \cdot d\mathbf{v}/dt, \tag{A.4}$$

where $p(0)$ is set to 0. Multiplying by $\mathbf{n}$ and integrating over the body surface gives

$$\oint -p\mathbf{n} ds = -\rho v \oint \left( \mathbf{n} \int_0^s \partial_n \omega ds \right) ds + \rho A_0 d\mathbf{v}/dt, \tag{A.5}$$

where $A_0 = \pi \cosh \mu_0 \sinh \mu_0$ is the area of the ellipse. Inserting Eqs. (8), (A.1) and (A.5) into Eq. (7), we have

$$(m - \rho A_0) \frac{dV_x}{dt} = \rho v \hat{\mathbf{e}}_x \cdot \oint \left( \omega \mathbf{s} - \mathbf{n} \int_0^s \partial_n \omega ds \right) ds. \tag{A.6}$$

Now we change variables to $(\mu, \theta)$, using

$$\mathbf{s} = \frac{1}{\sqrt{S}} \begin{pmatrix} -\cosh \mu_0 \sin \theta \\ \sinh \mu_0 \cos \theta \end{pmatrix}, \quad \mathbf{n} = \frac{1}{\sqrt{S}} \begin{pmatrix} \sinh \mu_0 \cos \theta \\ \cosh \mu_0 \sin \theta \end{pmatrix}$$

and $(dn, ds) = \sqrt{S}(d\mu, d\theta)$ on the body. Then Eq. (A.6) becomes

$$\frac{dV_x}{dt} = \frac{\rho v}{m - \rho A_0} \int_0^{2\pi} (-\omega \cosh \mu_0 \sin \theta + \partial_\mu \omega \sinh \mu_0 \sin \theta) d\theta. \tag{A.7}$$

## Appendix B. Vorticity boundary condition

Briley's formula [24] and the second-order version, Thom's formula [23], give expressions for the vorticity on the boundary in terms of the stream function on the boundary and in the interior of the domain. The formulae combine the statements of no-slip and no penetration with the statement that vorticity is equal to the Laplacian of the stream function, evaluated on the boundary.

Beginning in the 1970s, a number of researchers have avoided boundary vorticity formulae such as Briley's formula, for two main reasons.

(1) The local vorticity formulae can cause stability problems in explicit schemes, and convergence problems in implicit schemes [6].
(2) The vorticity boundary condition is not strictly equivalent to the no-slip condition.

Hence these authors [20,36] formulate the no-slip condition in terms of global compatibility conditions on the vorticity. Derived from Green's formula, these take the form of integral constraints on the vorticity, one constraint per boundary node. The historical development of these methods is described by Gresho [37], and recent implementations are given in [22]. Recently, E and Liu [38] have shown that two of the most commonly used global conditions are actually equivalent to local vorticity formulae. Theoretical work [39,40] continues in this area, though local vorticity formulae and global compatibility conditions give similar results for benchmark problems such as driven cavity flow [7] and the flow past a flat plate [41].

## Appendix C. Setting the far-field constant in the stream function

Let the fluid domain in the lab frame (at rest at infinity) be denoted $V(t)$. Then by the Transport Theorem [13],

$$\frac{d\Gamma}{dt} = \frac{d}{dt} \int_{V(t)} \omega dA = \int_{V(t)} \frac{D\omega}{Dt} dA. \tag{C.1}$$

By the vorticity Eq. (1) and the Divergence Theorem, this quantity equals

$$\int_{V(t)} \nu \Delta\omega \mathrm{d}A = -\int_{B(t)} \nu \partial_n \omega \mathrm{d}A, \tag{C.2}$$

where we denote the body by $B(t)$, and assume that $\omega$ decays like $o(1/r)$ in the far field (it decays exponentially for the flow past a body started from rest). By Eq. (A.3) this quantity becomes

$$-\int_{B(t)} \left( \frac{1}{\rho} \partial_s p + \mathbf{s} \cdot \mathrm{d}\mathbf{v}/\mathrm{d}t \right). \tag{C.3}$$

The integral of the first term in the integrand vanishes because the pressure is single-valued. The integral of the second term vanishes for a rectilinear motion. Hence the circulation is constant in time (equal to zero), and we use this relation to set $c_0$.

## Appendix D. Code verification

In this section we compare force coefficients for steady flows past an ellipse computed with the current scheme with those in the literature. In each comparison our results are converged with respect to refinement of the grid size and time step.

Dennis and Young [16] computed steady flow solutions past ellipses at moderate $Re$, inclined at various angles to the far-field flow. The main differences with our scheme are: (1) far-field boundary conditions which incorporate an asymptotic expansion for $\psi$, and (2) a different coordinate transformation.

In Table 2 we compare results for the lift and drag coefficients for the flow past an elliptical cylinder with aspect ratio $\tanh(0.2)$, inclined at various angles, at $Re = 20$. We find that our values are consistently within 1–2% of those in [16], which is the level of accuracy we are able to deduce for their results.

An earlier study by Lugt and Haussling [14] considered the flow past an impulsively started ellipse of aspect ratio $\tanh(0.1)$ with major axis inclined at 45° to the direction of motion. The main differences with our scheme are: (1) explicit time-stepping, (2) "out-flow" boundary conditions which allow the vorticity to advect through the downstream part of the computational boundary, and (3) a coarser mesh.

In Table 3, we compare our results for a thinner ellipse, $\mu_0 = 0.1$, inclined at 45° to the stream, at $Re = 15$ and 30. with those given in [16] and [14]. The latter work computes the time-dependent flow after an impulsive

Table 2
Validation of the code for a simple test case

| Angle | $C_L$ [16] | $C_L$ (present) | $C_D$ [16] | $C_D$ (present) |
|---|---|---|---|---|
| 20° | 0.735 | 0.742 | 1.295 | 1.293 |
| 40° | 0.936 | 0.932 | 1.598 | 1.601 |
| 60° | 0.698 | 0.689 | 1.904 | 1.903 |
| 80° | 0.253 | 0.249 | 2.084 | 2.080 |

Comparison of the lift coefficient ($C_L$, equal to the lift per unit width out-of-plane divided by $\rho U^2 L$) and drag coefficient ($C_D$) at $Re = 20$, with those presented in [16] for steady flow past an ellipse of aspect ratio $\tanh(0.2)$ at four angles of attack.

Table 3
Comparison of code with results from [14] and [16] for $C_L$ and $C_D$ at $Re = 15$ and 30, in steady flow past an ellipse of aspect ratio $\tanh(0.1)$ with major axis at 45° to the flow

| $Re$ | Work | $C_L$ | $C_D$ |
|---|---|---|---|
| 15 | Dennis and Young | 1.065 | 1.870 |
| 15 | Present | 1.051 | 1.873 |
| 30 | Lugt and Haussling ($t = 18$) | 0.955 | 1.45 |
| 30 | Lugt and Haussling ($t = 20.2$) | 0.940 | 1.44 |
| 30 | Dennis and Young | 0.941 | 1.406 |
| 30 | Present | 0.931 | 1.411 |

start, so we compare with the values at the latest times for which they are listed. Our results are consistently within 2% of the corresponding values from these works; the different initial conditions may account for this discrepancy.

## Appendix E. Convergence studies

Here we display the results of convergence tests with respect to the four numerical parameters $\Delta\mu, \Delta\theta, \Delta t, \mu_B$. We show how the main results of Section 4 vary with these parameters. In particular, we consider: (1) the growth rate of the envelopes in Figs. 2 and 3 and (2) the values of the horizontal fluid force $F_x$ and horizontal velocity $V_x$ of the body when $V_x$ is O(1).

To compute the growth rate of $V_x$ (see for example Fig. 5), we consider the time interval in which $10^{-12} \ll 10^{-8} \leqslant |V_x| \leqslant 10^{-2} \ll 1$, well-separated from the tolerance of the iterative method at $O(10^{-12})$, and from the O(1) regime. Within this time interval, we select a set of shorter time intervals with duration and starting time chosen from uniform distributions. The purpose is to average over the temporal fluctuations in the data. For each shorter interval, we compute the slope of the least-squares fit to the data on a log-linear plot. We then compute the mean ($\eta$) and the standard deviation ($\sigma$) for the slopes of all the intervals in the set.

We focus on a particular base case with $Re$ above $Re_{cr}$. The physical parameters are $Re = 11$, $M = 0.001$, $\mu_0 = 0.3$, $f = 1$, $A = \cosh(\mu_0)/2$. We then vary around a base set of numerical parameters: $m(= 2\pi/\Delta\theta) = 96$, $n = (\mu_B - \mu_0)/\Delta\mu = 96$, $\Delta t = 0.005$, $\mu_B = 6$.

### E.1. $\Delta\mu$-convergence

At least third-order convergence is expected for quantities involving the pressure force (see Eq. (19). In Table 4 we see that $n = 96$ is sufficient to obtain 1% accuracy in $\eta$, which is also the level of uncertainty, $\sigma/\eta$.

We also consider the effect of $n$ on quantities in the saturated regime. We use a start-up condition that initiates the saturated regime, similar to that given in Section 4. Here $V_x = 0.5(1 - e^{-(t/0.5)^2})$ for $0 \leqslant t < 0.5$, and $V_x$ is set by fluid forces (see Eq. (10)) for $t \geqslant 0.5$.

In Table 5 we display the relative error in $F_x$ at times $t = 0.01$ and 0.15, and in $V_x$ at $t = 2$, with respect to reference values computed for $n = 1024$ (for $F_x$) and $n = 256$ (for $V_x$). At $t = 0.01$, the relative error is large, likely due to the linear increase in $V_y$ (and thus discontinuous acceleration) at the start. A smoother increase in velocity can be used for improved accuracy. At $t = 0.15$, (when $F_x$ is largest), the relative error is much smaller than at $t = 0.01$, and remains significantly smaller for the remainder of the computation. The fourth and sixth columns give the ratio between the error and that for $n/2$. The values in parenthesis give the values corre-

Table 4
Linear growth rate versus $n$

| $n$ | $\eta$ | $\sigma/\eta$ |
|---|---|---|
| 72 | 3.7506e−01 | 5.3275e−03 |
| 96 | 3.8847e−01 | 3.1431e−03 |
| 128 | 3.9086e−01 | 6.1172e−03 |
| 144 | 3.9137e−01 | 8.0128e−03 |

Table 5
$\Delta\mu$-convergence in $F_x$ and $V_x$

| $n$ | $F_x(t = 0.01)$ | $F_x(t = 0.15)$ | Ratio | $V_x(t = 2)$ | Ratio |
|---|---|---|---|---|---|
| 64 | 3.1327e−01 | 3.1222e−02 | – | 1.8059e−01 | – |
| 96 | 1.0450e−01 | 7.9667e−03 | – | 4.9273e−02 | – |
| 128 | 1.8175e−02 | 2.8082e−03 | 11.1 (8–16) | 1.6893e−02 | 10.7 (9–17) |
| 192 | 1.9098e−02 | 5.8071e−04 | 13.7 (8–16) | 2.7891e−03 | 17.6 (13–23) |
| 256 | 1.6398e−02 | 1.6499e−04 | 17.0 (8–16) | – | – |
| 512 | 3.0217e−03 | 2.1736e−05 | 7.59 (9–17) | – | – |

sponding to third- and fourth-order convergence, assuming errors of the form $c\Delta\mu^k$, with the same value of $c$ for all $n$. Convergence between third- and fourth-order is found.

### *E.2. $\Delta\theta$-convergence*

Spectral-order convergence is expected (assuming a smooth underlying solution). In Table 6 we see that the relative error is nearly at the level of the statistical uncertainty $\sigma/\eta$ for $m = 80$, and is less than it for $m = 96$ and above. For the case of the prescribed start-up (Table 7), 64 modes are sufficient for good accuracy at this $Re$, due to the spectral convergence.

### *E.3. Second-order convergence in time step*

Second-order convergence is expected (see Eq. (16). In Table 8, the coarsest $\Delta t = 0.01$ agrees with the smaller time steps at the level of $\sigma/\eta$. For all of the results in this work we use $\Delta t = 0.005$. In Tables 9 and 10 we find second-order convergence in $F_x$ at $t = 0.5$, and in $V_x$ for $t \in [0, 12]$.

Table 6
Linear growth rate versus $m$

| $m$ | $\eta$ | $\sigma/\eta$ |
|---|---|---|
| 80 | 3.8702e−01 | 3.0104e−03 |
| 96 | 3.8870e−01 | 3.6024e−03 |
| 112 | 3.8882e−01 | 1.0447e−03 |
| 128 | 3.8890e−01 | 1.7175e−03 |

Table 7
$\Delta\theta$-convergence in $F_x$ and $V_x$

| $m$ | $\sup_{t\in[0,0.5]} \frac{\lvert F_x(t)-F_x^{256}(t)\rvert}{\lvert F_x^{256}(t)\rvert}$ | $\sup_{t\in[0,12]} \frac{V_x(t)-V_x^{128}(t)}{\lvert V_x^{128}(t)\rvert}$ |
|---|---|---|
| 64 | 1.9286e−09 | 1.5795e−03 |
| 96 | 1.6221e−11 | 6.2280e−05 |
| 128 | 1.4592e−11 | – |

Table 8
Linear growth rate versus $\Delta t$

| $\Delta t$ | $\eta$ | $\sigma/\eta$ |
|---|---|---|
| 1e−2 | 3.8916e−01 | 2.3137e−03 |
| 5e−3 | 3.8826e−01 | 1.9082e−03 |
| 2.5e−3 | 3.8965e−01 | 3.2117e−03 |

Table 9
$\Delta t$-convergence in $F_x$. $\tilde{F}_x$ denotes the value for $\Delta t = 6.25\text{e}-4$

| $\Delta t$ | $\sup_{t\in[0,0.5]} \frac{\lvert F_x(t)-\widetilde{F}_x(t)\rvert}{\lvert\widetilde{F}_x(t)\rvert}$ | Ratio | $\frac{\lvert F_x(0.5)-\widetilde{F}_x(0.5)\rvert}{\lvert\widetilde{F}_x(0.5)\rvert}$ | Ratio |
|---|---|---|---|---|
| 1e−2 | 1.0673e−01 | – | 1.0822e−03 | – |
| 5e−3 | 3.3463e−03 | 32 | 2.8261e−04 | 3.8 |
| 2.5e−3 | 1.3812e−03 | 2.4 | 6.9613e−05 | 4.1 |
| 1.25e−3 | 2.8867e−04 | 4.8 | 1.4167e−05 | 4.9 |

Ratio denotes the ratio of error for $\Delta t$ with that for $2\Delta t$.

Table 10
$\Delta t$-convergence in $V_x$. $\tilde{v}_x$ denotes the value for $\Delta t = 1.25\text{e}-3$

| $\Delta t$ | $\frac{\sup_{t\in[0,12]}\lvert V_x(t)-\widetilde{v}_x(t)\rvert}{\sup_{t\in[0,12]}\lvert\widetilde{v}_x(t)\rvert}$ | Ratio |
|---|---|---|
| 1e−2 | 8.6759e−02 | – |
| 5e−3 | 2.0068e−02 | 4.32 |
| 2.5e−3 | 4.9100e−03 | 4.09 |

Ratio denotes the ratio the error for $\Delta t$ with that for $2\Delta t$.

Table 11
Linear growth rate versus $\mu_B$

| $R = \text{e}^{\mu_B}/(\text{e}^{\mu_0} + \text{e}^{-\mu_0})$ | $\eta$ | $\sigma/\eta$ |
|---|---|---|
| 46.4 | 3.9021e−01 | 2.0211e−03 |
| 95 | 3.8871e−01 | 1.8952e−03 |
| 193 | 3.8773e−01 | 1.9988e−03 |
| 393 | 3.8868e−01 | 2.6988e−03 |

Table 12
$\mu_B$-convergence in $V_x$

| $R = \text{e}^{\mu_B}/(\text{e}^{\mu_0} + \text{e}^{-\mu_0})$ | $\frac{\sup_{t\in[0,12]}\lvert V_x(t)-\tilde{v}_x(t)\rvert}{\sup_{t\in[0,12]}\lvert\tilde{v}_x(t)\rvert}$ | Ratio |
|---|---|---|
| 46.4 | 2.6914e−03 | – |
| 95 | 6.4045e−04 | 4.20 (4.21) |
| 193 | 1.4775e−04 | 4.33 (4.32) |
| 393 | 2.8970e−05 | 5.10 (5.20) |

$\tilde{v}_x$ denotes the value for $R = 802$.

### *E.4. Outer boundary convergence*

A relative error of $\text{O}(\text{e}^{-2\mu_B})$ is expected in the outer boundary values of $\psi = \psi_B$ (see Section 3.2.2). In Table 11 we see that a distance of approximately 100 body radii is sufficient for accuracy at the level of the uncertainty, 0.2%. In Table 12 we show the error in $V_x$ over 12 flapping periods, for the start-up case. We use as a reference the solution for $R = 802$. The relative error in $\psi$ at the outer boundary is $\sim R^{-2}$, from Eq. (14). The values in the third column give the ratio of the error with that in the row above. The ratio is very close to that which would be expected for a leading-order error term $\sim R^{-2}$, given in parenthesis.

## References

[1] S.N. Fry, R. Sayaman, M.H. Dickinson, The aerodynamics of free-flight maneuvers in *Drosophila*, Nature 406 (2000) 94.
[2] J.C. Liao, D.N. Beal, G.V. Lauder, M.S. Triantafyllou, Fish exploiting vortices decrease muscle activity, Science 302 (5650) (2003) 1566–1569.
[3] N. Vandenberghe, J. Zhang, S. Childress, Symmetry breaking leads to forward flapping flight, J. Fluid Mech. 506 (2004) 147–155.
[4] N. Vandenberghe, S. Childress, J. Zhang, Hovering of a passive body in an oscillating airflow, Phys. Fluids 18 (2006) 117103.
[5] P.M. Gresho, Incompressible fluid dynamics: some fundamental formulation issues, Ann. Rev. Fluid Mech. 23 (1) (1991) 413–453.
[6] S.A. Orszag, M. Israeli, Numerical simulation of viscous incompressible flows, Ann. Rev. Fluid Mech. 6 (1974) 281–318.
[7] W.N. E, J.G. Liu, Essentially compact schemes for unsteady viscous incompressible flows, J. Comput. Phys. 126 (1) (1996) 122–138.
[8] Z.J. Wang, Vortex shedding and frequency selection in flapping flight, J. Fluid Mech. 410 (May) (2000) 323–341.
[9] A. Andersen, U. Pesavento, Z.J. Wang, Unsteady aerodynamics of fluttering and tumbling plates, J. Fluid Mech. 541 (2005) 65–90.
[10] S. Alben, M. Shelley, Coherent locomotion as an attracting state for a free flapping body, Proc. Nat. Acad. Sci. 102 (32) (2005) 11163–11166.
[11] L.A. Miller, C.S. Peskin, When vortices stick: an aerodynamic transition in tiny insect flight, J. Exper. Biol. 207 (17) (2004) 3073–3088.

[12] S. Childress, R. Dudley, Transition from ciliary to flapping mode in a swimming mollusc: flapping flight as a bifurcation in $Re_\omega$, J. Fluid Mech. 498 (2004) 257–288.
[13] L.M. Milne-Thomson, Theoretical Hydrodynamics, fifth ed., Macmillan, New York, 1968.
[14] H.J. Lugt, H.J. Haussling, Laminar flow past an abruptly accelerated elliptic cylinder at 45 degrees incidence, J. Fluid Mech. 65 (October) (1974) 711–734.
[15] M.H. Chou, An efficient scheme for unsteady flow past an object with boundary conformal to a circle, SIAM J. Sci. Stat. Comput. 13 (4) (1992) 860–873.
[16] S.C.R. Dennis, P.J.S. Young, Steady flow past an elliptic cylinder inclined to the stream, J. Eng. Math. 47 (2) (2003) 101–120.
[17] O.P. Iliev, M.M. Makarov, A block-matrix iterative numerical method for coupled solving of 2D Navier–Stokes equations, J. Comput. Phys. 121 (2) (1995) 324–330.
[18] Y. Saad, M.H. Schultz, GMRES-a generalized minimal residual algorithm for solving nonsymmetric linear systems, SIAM J. Sci. Stat. Comput. 7 (3) (1986) 856–869.
[19] Raz Kupferman, A central-difference scheme for a pure stream function formulation of incompressible viscous flow, SIAM J. Sci. Comput. 23 (1) (2001) 1–18.
[20] L. Quartapelle, Numerical Solution of the Incompressible Navier–Stokes Equations, first ed., Birkhauser, Basel, Switzerland, 1993.
[21] P.F.D. Mancera, R. Hunt, Fourth-order method for solving the Navier–Stokes equations in a constricting channel, Int. J. Numer. Meth. Fluids 25 (10) (1997) 1119–1135.
[22] R. Peyret, Spectral Methods for Incompressible Viscous Flow, first ed., Springer, New York, 2002.
[23] A. Thom, The flow past circular cylinders at low speeds, Proc. Roy. Soc. Lond. Ser. A A141 (1933) 651–669.
[24] W.R. Briley, Numerical study of laminar separation bubbles using Navier–Stokes equations, J. Fluid Mech. 47 (1971) 713.
[25] H.X. Huang, B.R. Wetton, Discrete compatibility in finite difference methods for viscous incompressible fluid flow, J. Comput. Phys. 126 (2) (1996) 468–478.
[26] C.R. Anderson, M.B. Reider, A high order explicit method for the computation of flow about a circular cylinder, J. Comput. Phys. 125 (1) (1996) 207–224.
[27] D.W. Peaceman, H.H. Rachford Jr., The numerical solution of parabolic and elliptic differential equations, J. Soc. Ind. Appl. Math. 3 (1) (1955) 28–41.
[28] L.S. Pan, Y.T. Chew, A general formula for calculating forces on a 2-D arbitrary body in incompressible flow, J. Fluid. Struct. 16 (1) (2002) 71–82.
[29] M. Jenny, G. Bouchet, J. Dusek, Nonvertical ascension or fall of a free sphere in a Newtonian fluid, Phys. Fluids 15 (1) (2003) L9–L12.
[30] B. Pier, On the frequency selection of finite-amplitude vortex shedding in the cylinder wake, J. Fluid Mech. 458 (2002) 407–417.
[31] E. Kelley, M.M. Wu, Path instabilities of rising air bubbles in a Hele-Shaw cell, Phys. Rev. Lett. 79 (7) (1997) 1265–1268.
[32] A. Belmonte, H. Eisenberg, E. Moses, From flutter to tumble: inertial drag and froude similarity in falling paper, Phys. Rev. Lett. 81 (2) (1998) 345–348.
[33] D. Shiels, A. Leonard, A. Roshko, Flow-induced vibration of a circular cylinder at limiting structural parameters, J. Fluid. Struct. 15 (1) (2001) 3–21.
[34] P.W. Bearman, Vortex shedding from oscillating bluff bodies, Ann. Rev. Fluid Mech. 16 (1984) 195–222.
[35] H. Aref, Integrable, chaotic, and turbulent vortex motion in two-dimensional flows, Ann. Rev. Fluid Mech. 15 (1983) 345–389.
[36] R. Glowinski, O. Pironneau, Numerical methods for the 1st biharmonic equation and for the 2-dimensional Stokes problem, SIAM Rev. 21 (2) (1979) 167–212.
[37] P.M. Gresho, Some interesting issues in incompressible fluid dynamics both in the continuum and in numerical simulation, Adv. Appl. Mech. 28 (1992) 45–140.
[38] W. E, J.G. Liu, Vorticity boundary condition and related issues for finite difference schemes, J. Comput. Phys. 124 (2) (1996) 368–382.
[39] C. Wang, J.G. Liu, Analysis of finite difference schemes for unsteady Navier–Stokes equations in vorticity formulation, Numer. Math. 91 (3) (2002) 543–576.
[40] T.Y. Hou, B.T.R. Wetton, Convergence of a finite-difference scheme for the Navier–Stokes equations using vorticity boundary conditions, SIAM J. Numer. Anal. 29 (3) (1992) 615–639.
[41] S.C.R. Dennis, Q. Wang, M. Coutanceau, J.L. Launay, Viscous flow normal to a flat plate at moderate Reynolds numbers, J. Fluid Mech. 248 (March) (1993) 605–635.